



## Electrochemical properties of ultrasonically prepared $\text{Ni}(\text{OH})_2$ nanosheets in lithium cells



A. Caballero<sup>a</sup>, L. Hernán<sup>a,\*</sup>, J. Morales<sup>a</sup>, S. Cabanas-Polo<sup>b</sup>, B. Ferrari<sup>b,\*\*</sup>,  
A.J. Sanchez-Herencia<sup>b</sup>, J. Canales-Vázquez<sup>c</sup>

<sup>a</sup> Instituto Universitario de Investigación en Química Fina y Nanoquímica, Dpto. Química Inorgánica, Campus de Rabanales, Universidad de Córdoba, 14071 Córdoba, Spain

<sup>b</sup> Instituto de Cerámica y Vidrio (ICV-CSIC), C/Kelsen 5, 28049 Madrid, Spain

<sup>c</sup> Instituto de Energías Renovables, Paseo de La Investigación 1, Universidad de Castilla-La Mancha, 02071 Albacete, Spain

### H I G H L I G H T S

- Electrochemical properties of  $\text{Ni}(\text{OH})_2$  nanosheets in lithium cells are described.
- The nanosheets were prepared by a special method to stabilize particle growth.
- The electrode provides a high specific capacity ( $1350 \text{ mAh g}^{-1}$ ).
- We ascribe this capacity excess to the SEI formation.
- The good capacity retention of the electrode is indicative of its reversibility.

### A R T I C L E I N F O

#### Article history:

Received 25 October 2012

Received in revised form

23 February 2013

Accepted 7 April 2013

Available online 19 April 2013

#### Keywords:

Nickel hydroxide

Nanosheets

Lithium batteries

Solid–electrolyte interface

### A B S T R A C T

The electrochemical behavior of  $\beta\text{-Ni}(\text{OH})_2$  nanosheets in half-lithium cells was studied. The first discharge curve exhibited two well-defined plateaux giving two well-defined peaks in the CV curve. The plateaux were assigned to reduction of Ni in the nanosheets to metallic Ni and the formation of a solid electrolyte interface (SEI), respectively. By contrast, NiO exhibited a single peak. On further cycling, the curve shapes for  $\beta\text{-Ni}(\text{OH})_2$  resembled those for NiO, but the peak assigned to Ni oxidation was shifted to higher voltages. Cycling the electrode made from the nanosheets over the potential range 3.0–0.0 V provided capacities above  $1430 \text{ mAh g}^{-1}$  after the second cycle that were largely retained on further cycling. This surprisingly high capacity level substantially exceeds the theoretical capacity of  $\text{Ni}(\text{OH})_2$  and is twice the theoretical value for NiO. Removing the plateau assigned to SEI formation by limiting the lower potential to 0.85 V caused not only the expected decrease in discharge capacity, but also substantial capacity fading with cycling, which provides direct evidence for the central role of SEI formation. The unusually high capacity obtained is probably due to formation of the reversible interface as demonstrated by transmission electron microscopy (TEM) images of the discharged and charged electrode.

© 2013 Elsevier B.V. All rights reserved.

## 1. Introduction

Finding anode materials with a reversible capacity well above that of graphite ( $372 \text{ mAh g}^{-1}$ ) is one of the major approaches to increasing the specific energy of Li-ion batteries [1]. The materials possessing this property include transition metal oxides, which have been extensively studied in this respect ever since their reversible

electrochemical reactivity toward Li was discovered by Tarascon's group [2]. Especial attention in this respect has been given to NiO prepared in a wide variety of shapes and textures [3–14]. Specific capacities close to the theoretical value for this oxide,  $718 \text{ mAh g}^{-1}$ , can usually be obtained at moderate current intensities. By contrast,  $\text{Ni}(\text{OH})_2$  has received comparatively little attention, probably as a result of its containing  $\text{OH}^-$  ions, which may be reactive toward the chemicals in a battery. Recently,  $\text{Ni}(\text{OH})_2$ /graphene composites were proposed as novel lithium storage materials; these composites deliver specific capacities above  $1400 \text{ mAh g}^{-1}$  [15], which, however, fade considerably on cycling. In any case, this proposal ignores a potential role of the graphene.

\* Corresponding author. Fax: +34 957218621.

\*\* Corresponding author.

E-mail addresses: [iq1hepal@uco.es](mailto:iq1hepal@uco.es) (L. Hernán), [bferrari@icv.csic.es](mailto:bferrari@icv.csic.es) (B. Ferrari).

In this work, we studied the electrochemical behavior of pure  $\beta$ -Ni(OH)<sub>2</sub> in lithium cells. The hydroxide was obtained with a special method using ultrasound and surfactants in combination to ensure uniform particle growth. The preliminary results obtained in this work were rather encouraging. Thus, Ni(OH)<sub>2</sub> particles delivered capacities markedly exceeding the theoretical value for NiO and exhibited surprisingly good capacity retention on cycling.

## 2. Experimental

Pure Ni(OH)<sub>2</sub> in its  $\beta$ -form was synthesized from Ni(NO<sub>3</sub>)<sub>2</sub>·6H<sub>2</sub>O and NH<sub>4</sub>OH, using a high intensity ultrasonic horn and polyvinylpyrrolidone (PVP) in an Ni<sup>2+</sup>/PVP mole ratio of 100:1 as surfactant. The synthesis conditions used are described in detail elsewhere [16]. TEM images were recorded using a JEOL 2100 electron microscope operating at 200 kV and equipped with an Orius Gatan CCD camera. Specimens for TEM were prepared by depositing few drops of a hexane-based suspension of the charged and discharged samples onto a holey-carbon Cu grid under vacuum. Imaging was carried out under low beam irradiation conditions to avoid degradation of the samples inside the TEM column. Electrochemical measurements were made on 2032 coin-type cells. The electrodes were prepared by mixing the hydroxide with 20% carbon black and depositing the mixture onto copper foil (13 mm in diameter) by using the doctor blade technique. The mass of Ni(OH)<sub>2</sub> used was 5 mg cm<sup>-2</sup>. Adherence of active particles to the substrate was quite good and made adding a binder to prepare the electrode redundant. Lithium metal was used as counter electrode. The electrolyte was 1 M LiPF<sub>6</sub> in a 1:1 mixture of ethylene carbonate and dimethyl carbonate. Cells were assembled in an M-Braun glove box under an argon atmosphere. Constant current tests were performed on an Arbin BT2000 multichannel potentiostat–galvanostat. Cyclic voltammograms (CV) were obtained at different scan rates on a Solartron Instrument model 1470E. All measurements were made in duplicate in order to ensure accuracy in the electrochemical tests.

## 3. Results and discussion

As confirmed by its XRD pattern (Fig. 1),  $\beta$ -Ni(OH)<sub>2</sub> was obtained as a highly pure phase. The solid was indexed in the hexagonal

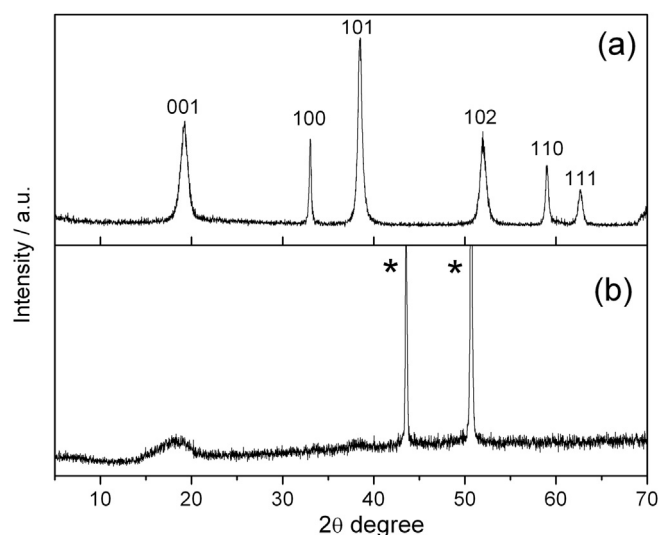


Fig. 1. XRD pattern for  $\beta$ -Ni(OH)<sub>2</sub> before (a) and after of discharging the electrode to 0.85 V (b). (\*) Peaks belonging to Cu substrate.

system and its calculated lattice parameters were  $a = 3.128(7)$  Å and  $c = 4.619(8)$  Å, both of which are consistent with other values previously reported in JCPDS. The sample exhibited broad peaks associated with a small crystallite size. The well-known Scherrer formula was used to calculate crystallite size along the  $c$  and  $a$  axes from the peak position and full width at half maximum of the (001) and (100) reflections, respectively. The results are shown in Table 1 together with other properties such as density, specific surface area and particle diameter as calculated from the latter parameter. Worth special note is the low crystallite size, which was greater along the [100] direction and quite similar to the theoretical BET diameter. Fig. 2 shows TEM images of the powders as obtained at variable magnification for the basal and perpendicular planes. As can be seen from Fig. 2a,  $\beta$ -Ni(OH)<sub>2</sub> was obtained as platelet-like particles. This was a result of strong preferential absorption of the surfactant on the (001) plane in the nickel hydroxide structure. Calculating the size of the particles from the TEM images was made difficult by their tendency to agglomerate. In any case, platelets in diameters around 50 nm or even smaller and a few nanometers thick prevailed. This size is quite similar to the theoretical BET diameter of Table 1. Higher magnification (Fig. 2b and c) revealed substantial disorder along the [010] and [001] directions.

Fig. 3a shows selected discharge/charge curves recorded at 100 mA g<sup>-1</sup> (0.17 C, with  $C = 718$  mA g<sup>-1</sup>) over the voltage range 3.0–0.0 V. The specific capacity for the first discharge was around 2000 mAh g<sup>-1</sup>, which is much higher than the theoretical value (578 mAh g<sup>-1</sup>) if complete reduction of Ni<sup>2+</sup> to Ni<sup>0</sup> is assumed. The curve exhibits two well-defined plateaux the first of which delivers a capacity around 600 mAh g<sup>-1</sup> and can be ascribed to collapse of the hydroxide layer structure and conversion into Ni via the reaction



Ni(OH)<sub>2</sub> decomposition was confirmed by the ex-situ XRD pattern of the electrode cut at 0.85 V (Fig. 1b). As can be seen, the strongest peaks for the pristine compound were barely discernible and all others disappeared altogether. The residual presence of the (001) reflection is caused by the layered morphology of the nano-sheets and its width reflects the strong structural disorder underwent by reaction with lithium. Therefore, most Ni(OH)<sub>2</sub> particles were converted into Ni. However, no peaks for the element were visible. This is consistent with the nanosized nature and low crystallinity of the metal particles formed by electrochemical reduction of transition metal oxides in Li cells and also with the difficulty of detecting them with X-ray powder methods [17,18]. The second plateau, located at ca. 0.7 V, can be ascribed to formation of the solid electrolyte interface (SEI). This curve shape is rather different from that for NiO, which usually consists of a single, extended plateau at 0.6 V consistent with the reaction



and simultaneous formation of the SEI layer [3–5,9–13]. The charge curve is strongly polarized and its shape quite similar to that for the NiO curve, which is consistent with formation of Ni from the hydroxide. For better description of the curve profiles, Fig. 3b shows the corresponding differential capacity plots, where the plateaux appear as peaks. The two broad, weak peaks at ca. 1.6 and 2.3 V

Table 1  
Crystallite size, density, specific surface area and BET diameter of  $\beta$ -Ni(OH)<sub>2</sub>.

$L_{001}$ (nm)	$L_{100}$ (nm)	$\rho$ (g cm <sup>-3</sup> )	SSA (m <sup>2</sup> g <sup>-1</sup> )	$D_{\text{BET}}$ (nm)
8.8	29.0	3.8	52.0	30.2

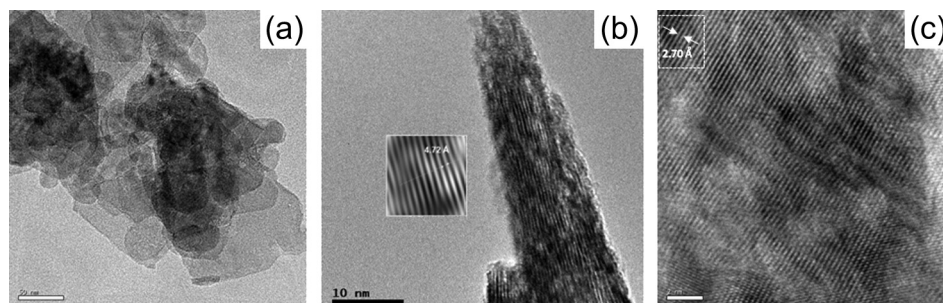


Fig. 2. (a) TEM image of  $\beta$ -Ni(OH) $_2$ . HRTEM images along the [100] (b) and [001] directions (c).

must correspond to dissolution of the organic SEI layer and oxidation of Ni nanograins, respectively [4,5,7,8,19,20].

Subsequent discharge curves were quite similar to one another and exhibited a strong asymmetric peak around 1.2 V. No such asymmetry is observed in the curves for NiO [3–5,9–13], which, to our minds, contributes significantly to the unexpected performance of Ni(OH) $_2$ -based cells. The shape of the charge curves changed little over the first few cycles. In the fifth, the curves exhibited a slope change above 2.5 V reflecting in a peak at ca. 2.8 V in the differential capacity plots. The intensity of this new peak increased as that of the peak at ca. 2.3 V decreased on cycling.

CV curves (Fig. 4) provided supplementary information on the electrochemical properties derived from Fig. 3b. Thus, the first cathodic scan revealed a strong peak at ca. 0.85 V followed a weaker peak at ca. 0.65 V, the two being consistent with the plateaux in the galvanostatic curve (Fig. 3a). As noted earlier, these peaks

correspond to the initial reduction of Ni(OH) $_2$  to metallic Ni, with Li(OH) and SEI formation. Again, the first cathodic scan for NiO only gave a single peak and this was assigned to reaction (2) and formation of the SEI layer. In other words, SEI formation in the hydroxide reduction was more apparent and occurred at a different potential than the hydroxide reduction. A complex signal at 1.1–2.0 V consisting of at least two peaks was observed during the first anodic scan, followed by a stronger, rather symmetric peak at 2.3 V. This curve shape is quite similar to that for NiO [3–14]. The complex signal obtained must correspond to dissolution of the organic SEI layer [18,19] and the strong peak at 2.3 V to the decomposition of Li $_2$ O and the formation of NiO [4,5,7,8,19,20]. The second cathodic scan exposed significant changes and contained a strong, broad, asymmetric peak at ca. 1.15 V as its most salient feature. No especially significant changes were observed in the following cathodic scans except for greater peak symmetry. By contrast, the anodic scans exhibited noteworthy changes. Thus, the peak assigned to Ni oxidation was shifted to higher potentials and decreased in intensity — seemingly, a new peak developed at ca. 2.8 V at its expense. No similar changes have been observed in the CV curves for NiO [3–13] and, to our knowledge, they are typical of Ni(OH) $_2$ . The CV curves were consistent with the galvanostatic curves as regards electrochemical properties, and interestingly the unexpected high pseudo-plateaux observed on the galvanostatic charge curves after the first few cycles.

Ex-situ TEM studies of the electrode in the charged and discharged states provided complementary information on the reversibility of the NiO conversion reaction. Moreover, they offered a better identification of the phases formed, taking into account the difficulty shown by the XRD patterns due to a severe reduction of

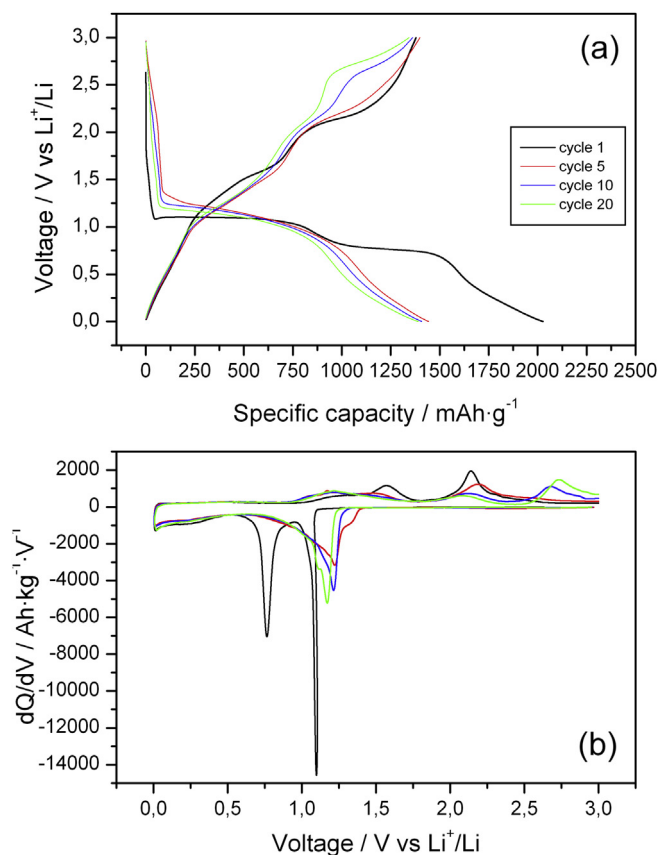


Fig. 3. (a) Galvanostatic discharge–charge curves for  $\beta$ -Ni(OH) $_2$  as recorded in different cycles. Current density 100 mA g $^{-1}$ , voltage range 3.0–0.0 V. (b) Differential capacity plots for the galvanostatic curves.

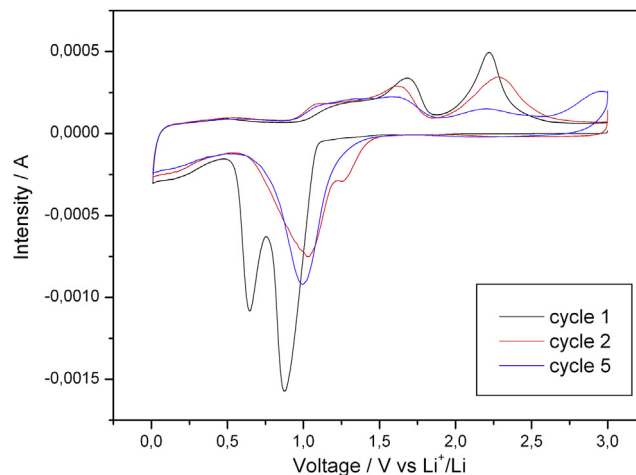


Fig. 4. Cyclic voltammograms for the  $\beta$ -Ni(OH) $_2$ /Li half-cell at a scan rate of 0.1 mV s $^{-1}$ . Cycle numbers are shown in the graph.



the particle size together with a significant loss of crystallinity. For this study we selected the discharged and charged electrode at the fifth cycle, where the half-cell was reasonably stabilized (the shape of the charge and discharge curve become invariable). Fig. 5 shows some TEM images of the discharged (Li insertion) and charged electrode (Li deinsertion). The low magnification image of the discharged electrode, Fig. 5a, revealed the presence of rather dispersed bright and dark nanoparticles embedded in a fairly transparent matrix. The SAED (Fig. 5b) exhibited weak, diffuse rings, which agrees with the polycrystalline nature of the specimen. The three more intense rings can be indexed as the reflections (111) of  $\text{Li}_2\text{O}$  and (111) and (200) of metallic Ni. According with these results, the dark nanoparticles can be unambiguously assigned to Ni metal, whilst the brighter nanoparticles are  $\text{Li}_2\text{O}$ . The HRTEM images of the dark nanoparticles (Fig. 5c) showed fringes of ca. 2 Å, in good agreement with the spacing of the {111} planes of Ni. Occasionally, fringes of 4.6 Å were observed consistent with the spacing of the {111} planes of  $\text{Li}_2\text{O}$  (Fig. 5d). We were unable to identify the LiOH phase, either because it may dehydrate under the electron beam or during the electrochemical process itself.

The images of the charge electrode (Li deinsertion) were quite different as the particles underwent significant morphology changes. As can be seen in the low magnification image of Fig. 5e, the particles morphology was quite similar to the platelets morphology of the parent compound (see Fig. 2a). The corresponding selected area electron diffraction pattern (SAED) revealed clearly the presence of reflections that corresponded to the [100] direction in NiO (Fig. 5f). Although ( $h00$ ), with  $h = 2n + 1$ , reflections are forbidden by symmetry, they appeared in this case probably due to kinematic effects. Nevertheless, there also appeared some weak reflections and diffuse scattering consistent with the nanoparticles mosaic and with the main structural features of NiO. The HRTEM image (Fig. 5g) revealed that the nano-sheets were formed by multiple interconnected crystalline nanodomains (below 10 nm in size) randomly oriented, which exhibited lattice fringes with spacings in good agreement with NiO interplanar distances. The Fast Fourier Transform (FFT) image, Fig. 5h, is consistent with this statement.

Fig. 6 shows the capacity delivered by the electrode in the 3.0–0.0 V range as a function of the number of cycles. Apart from

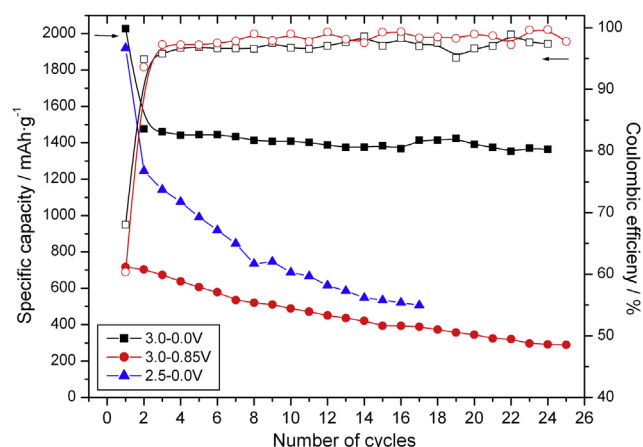


Fig. 6. Cycling properties of  $\beta\text{-Ni(OH)}_2$ . Voltage range: (■ black) 3.0–0.0 V; (● red) 3.0–0.85 V; (▲ blue) 2.5–0.0 V. The coulombic efficiency in the voltage range 3.0–0.0 V is also included. (For interpretation of the references to colour in this figure legend, the reader is referred to the web version of this article.)

the irreversible capacity observed in the first cycle, these systems exhibited a common feature: the delivered capacity remained very high on further cycling (around  $1430 \text{ mAh g}^{-1}$ , which is about  $730 \text{ mAh g}^{-1}$  higher than the theoretical capacity of NiO, in the second cycle). We only know of a single reported value exceeding the theoretical capacity of this oxide, and only by  $80 \text{ mAh g}^{-1}$  [5]. Moreover, capacity retention was not as good as here (about 0.32% of the capacity was lost in each cycle). Except for the first few cycles, the coulombic efficiency (Fig. 6) was 98% on average, which is consistent with the good reversibility of the electrochemical reactions undergone by the electrode during the discharge and charge processes.

As noted earlier, the reactivity of  $\text{Ni(OH)}_2$  and NiO in lithium cells differs mainly in the potential for conversion into Ni and in the presence of a well-defined plateau in the first discharge curve for  $\text{Ni(OH)}_2$  that can be assigned to SEI formation. The role played by these secondary reactions was examined by preventing formation of the SEI layer. Fig. 7 shows the charge/discharge curves for the

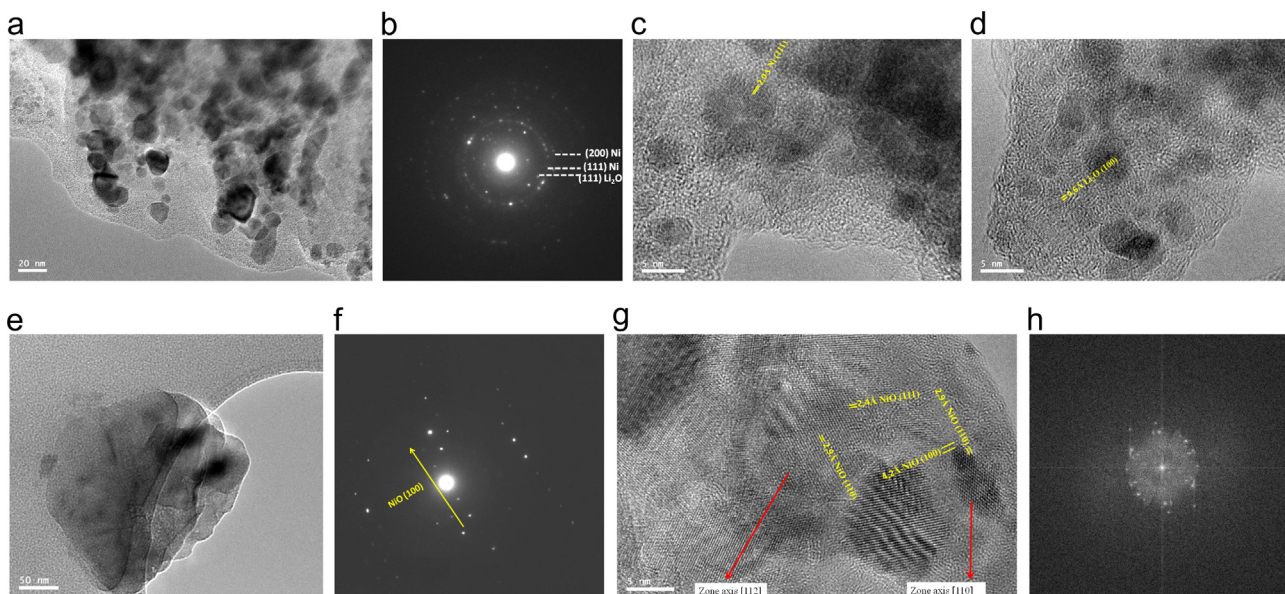


Fig. 5. TEM and SAED images of the discharged (a–d) and charged (e–h) electrode at the fifth cycle.

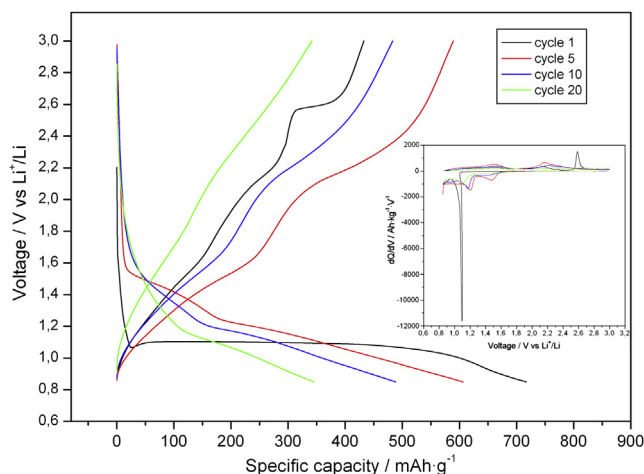


Fig. 7. Galvanostatic discharge–charge curves for  $\beta$ -Ni(OH) $_2$  as recorded in different cycles. Current density 100 mA g $^{-1}$ , voltage range 3.0–0.85 V. The inset shows the corresponding differential capacity plots.

ensuing half-cell on cycling from 3.0 to 0.85 V. A substantial difference in shape was observed in relation to the curves of Fig. 3a and b, especially in the discharge branch. Thus, after the first cycle, the strong cathodic peak split into two the potentials of which changed with the number of cycles. Also, retention of the delivered capacity — which was obviously lower than that of the half-cell tested to 0.0 V — on cycling was rather poor (see Fig. 6). Therefore, blocking SEI formation by suppressing the low voltage plateau in the discharge branch detracted from electrode performance. In other words, formation of the SEI layer ensured good cycling stability in the electrode.

Similar tests were conducted to examine the role of the anodic peak at 2.8 V observed after the first few cycles. Fig. 8 shows the charge/discharge curves obtained by cycling from 2.5 to 0.0 V. Although changes in curve shape — particularly in the discharge branch — were not so marked as those observed by limiting the capacity to 0.85 V (see Fig. 7), a dramatic reduction in plateau width in the discharge curve upon cycling was the main effect. This result may reflect a shift in Ni oxidation to higher potentials with cycling. In any case, the result is similar to that obtained by limiting the potential, namely: rapid fading of the discharge capacity in the first

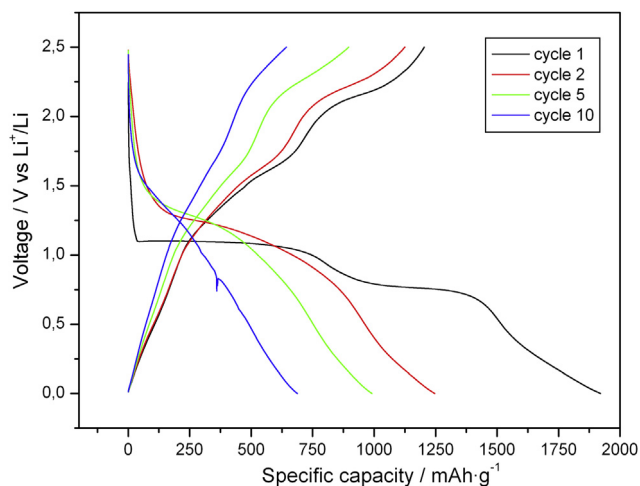
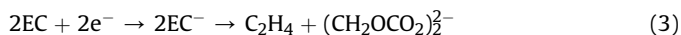


Fig. 8. Galvanostatic discharge–charge curves for  $\beta$ -Ni(OH) $_2$  as recorded in different cycles. Current density 100 mA g $^{-1}$ , voltage range 2.5–0.0 V.

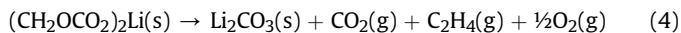
ten cycles and leveling off at ca. 500 mAh g $^{-1}$  on further cycling (see Fig. 6). Thus, limiting the upper and lower voltage of the range (or, in other words, suppressing the higher and lower potential plateau) significantly degrades electrode performance. In fact, the capacity delivered by the half-cell was even lower than the theoretical capacity.

There remains an open question: what is the origin of the additional capacity delivered by the Ni(OH) $_2$ -based electrode? The answer is not easy, but may be provided by these two major differences from the electrochemical response of NiO: (i) the reduction potential of the two compounds, which differs as a consequence of their dissimilar structure, may affect Ni reactivity; and (ii) the presence of OH $^-$  ions may influence the nature of the electrolyte decomposition products. One other singularity of this compound is its special particle morphology: very thin nanoplatelets approximately 50 nm in diameter. In fact, the electrochemical performance of micro-sized Ni(OH) $_2$  rechargeable alkaline batteries was previously found to be substantially improved by the addition of nanosized Ni(OH) $_2$  [21].

Although the composition of the SEI cannot be unambiguously established owing to the large number of factors involved in its formation, there is abundant literature about the reduced species proposed — and experimentally confirmed in some cases [22]. The latter include Li aryl carbonates such as (CH $_2$ OCO $_2$ ) $_2$ Li $_2$  and ROCO $_2$ Li, which are formed by nucleophilic attack on the solvents [23].



Similar reactions have been proposed for other solvents such as DMC or DEC [24]. Lithium aryl carbonate species can decompose according to reactions such as [25]



Also, O $_2$  and CO $_2$  can be reduced to form Li $_2$ O and Li $_2$ CO $_3$  [24]:



All these reactions may contribute to the additional capacity of the Ni(OH) $_2$  electrode (ca. 1430 mAh g $^{-1}$  in the first discharge, Fig. 3). Although part of this capacity is irreversible, a significant fraction is retained over prolonged cycling. In other words, there must exist some mechanism capable of hindering formation of the Li $_2$ CO $_3$  stable phase and inadequate to be reduced. One plausible mechanism involves OH $^-$  ions. Thus, this species may stabilize anionic intermediates such as aryl carbonates species, thereby hindering reaction (3) — and hence (4) and (5). One other mechanism involves the catalytic activity of metallic nanoparticles, which, according to Tarascon et al. [19], may make SEI formation and decomposition partially reversible. The latter mechanism is quite plausible here if one considers the high structural disorder and the low crystallinity of Ni formed (see Fig. 5a, c and d).

In this context, the TEM images of Fig. 5 were very valuable. As described above, the active particles formed during the discharge process (Ni and Li $_2$ O) were embedded in the matrix, which could be identified as a Li aryl carbonate as suggested by its amorphous structure. Thus, the amorphous matrix should derive from the reduction of the electrolyte upon discharging the cell (Eq. (3)). On charging the cell, this amorphous matrix tended to disappear, restoring the platelet morphology of the particles (see Fig. 5d and f). In other words, the aryl carbonate intermediates formed are prone to oxidation on charging of cell (reverse of reaction (3)). Therefore,

the TEM images demonstrated the reversibility of the side reactions undergone by the electrolyte and explain why the delivered capacity by the electrode exceeds to the theoretical capacity of NiO and its coulombic efficiency is close to 100% (see Fig. 6). The shoulder on the left of the reduction peak and the low voltage oxidation peak observed in the discharge and charge branches, provided complementary data for reaction (3) in its forward and reverse direction, respectively, and hence for reversibility in the SEI formation process.

## 5. Conclusions

Nickel hydroxide nanosheets provide an excellent electrochemical response in lithium cells as revealed by the high specific capacity delivered after 25 cycles: above  $1350 \text{ mAh g}^{-1}$  at a moderate current intensity ( $100 \text{ mA g}^{-1}$ ). This capacity level markedly exceeds the theoretical value for NiO ( $718 \text{ mAh g}^{-1}$ ), which forms after the first charge cycle. The additional capacity can be ascribed to secondary reactions involving SEI formation, which occurs in most anode materials — and, as clearly apparent from the galvanostatic curves at ca. 0.7 V, also in this hydroxide. The most salient feature of this material is that the reaction remains reversible on charging of the cell. We believe that such an uncommon behavior must be the result of catalytic activity in the Ni particles — which must be very small judging by the morphology of the pristine hydroxide and the lack of reflections in its XRD pattern. SAED patterns confirmed the reversibility of the  $\text{NiO} \leftrightarrow \text{Ni}$  conversion and the TEM images shed additional light on the reversibility of the secondary reactions undergone by the electrolyte.

## Acknowledgement

We acknowledge funding from Spain's Ministry of Science and Innovation (Projects MAT2009-14408-C02-01, MAT2008-03160

and MAT2011-27110) and the Andalusian Regional Government (Group FQM-175).

## References

- [1] M. Armand, J.M. Tarascon, *Nature* 451 (2008) 652.
- [2] P. Poizot, S. Laruelle, S. Grugeon, L. Dupont, J.M. Tarascon, *Nature* 407 (2000) 496.
- [3] S.A. Needham, G.X. Wang, H.K. Liu, J. Power Sources 159 (2006) 254.
- [4] X.H. Huang, J.P. Tu, B. Zhang, C.Q. Zhang, Y. Li, Y.F. Yuan, H.M. Wu, J. Power Sources 161 (2006) 541.
- [5] B. Varghese, M.V. Reddy, Z. Yanwu, C.S. Lit, T.C. Hoong, G.V. Subba Rao, B.V.R. Chowdari, A.T.S. Wee, C.T. Lim, C.H. Sow, *Chem. Mater.* 20 (2008) 3360.
- [6] X. Li, A. Dhanabalan, K. Bechtold, C. Wang, *Electrochem. Commun.* 12 (2010) 1222.
- [7] X.H. Huang, J.P. Tu, C.Q. Zhang, F. Zhou, *Electrochim. Acta* 55 (2010) 8981.
- [8] Y.F. Yuan, X.H. Xia, J.B. Wu, J.L. Yang, Y.B. Chen, S.Y. Guo, *Electrochem. Commun.* 12 (2010) 890.
- [9] C. Wang, D. Wang, Q. Wang, H. Chen, J. Power Sources 195 (2010) 7432.
- [10] X. Wang, X. Li, X. Sun, F. Li, Q. Liu, Q. Wang, D. He, J. Mater. Chem. 21 (2011) 3571.
- [11] X. Li, A. Dhanabalan, C. Wang, J. Power Sources 196 (2011) 9625.
- [12] H. Liu, G. Wang, J. Liu, S. Qiao, H. Ahn, J. Mater. Chem. 21 (2011) 3046.
- [13] X. Chen, N. Zhang, K. Sun, *Electrochem. Commun.* 20 (2012) 137.
- [14] B. Wang, J.L. Cheng, Y.P. Wu, D. Wang, D.N. He, *Electrochem. Commun.* 23 (2012) 5.
- [15] B. Li, H. Cao, J. Shao, H. Zheng, Y. Lu, J. Yin, M. Qu, *Chem. Commun.* 47 (2011) 3159.
- [16] S. Cabanas-Polo, K.S. Suslick, A.J. Sánchez-Herencia, *Ultrason. Sonochem.* 18 (2011) 901.
- [17] S. Grugeon, S. Laruelle, L. Dupont, J.M. Tarascon, *Solid State Sci.* 5 (2005) 895.
- [18] J.S. Do, C.H. Weng, J. Power Sources 146 (2005) 482.
- [19] S. Grugeon, S. Laruelle, R. Herrera-Urbina, L. Dupont, P. Poizot, J.M. Tarascon, *J. Electrochem. Soc.* 148 (2001) A285.
- [20] A. Debart, L. Dupont, P. Poizot, J.B. Leriche, J.M. Tarascon, *J. Electrochem. Soc.* 148 (2001) A1266.
- [21] X. Liu, L. Yu, J. Power Sources 128 (2004) 326.
- [22] P. Verma, P. Maire, P. Novak, *Electrochim. Acta* 55 (2010) 6332.
- [23] D. Aurbach, B. Markovsky, A. Shechter, Y. Ein-Eli, *J. Electrochem. Soc.* 143 (1996) 3809.
- [24] P. Arora, R.E. White, M. Doyle, *J. Electrochem. Soc.* 145 (1998) 3647.
- [25] A.M. Andersson, K. Edström, *J. Electrochem. Soc.* 148 (2001) A1100.